

PHOTODISSOCIATION DYNAMICS OF HONO(\tilde{A}): VELOCITY ALIGNED DOPPLER SPECTROSCOPY OF THE OH FRAGMENT

Richard N. DIXON and Hugh RIELEY¹
School of Chemistry, The University, Bristol BS8 1TS, UK

Received 6 February 1989; in final form 14 June 1989

High resolution line profiles of the OH fragment ejected by HONO(\tilde{A}), prepared with either one or two quanta in its terminal N=O mode, have been recorded in velocity aligned Doppler spectroscopy (VADS). Tightly collimated and counter-propagating photolysis and pulse-amplified probe beams were time delayed to yield the OH fragment speed distribution and, by conservation of energy and momentum, the internal energy distribution in the NO partner. The profiles following dissociation of HONO(2^2) are consistent with the NO internal distribution determined in a direct study of the NO fragment. Photodissociation of HONO(2^1) revealed a wide internal energy distribution in the NO and the lack of a significant population in NO($v''=0$). The observations are rationalised on terms of an \tilde{A} state potential energy surface which is quasi-stable in the N=O coordinate and essentially repulsive along the O–N coordinate. The utility of VADS and its wider applicability are discussed.

1. Introduction

A detailed analysis of the fragment energy distribution characterises the “end point” of photodissociation and provides an insight into the later dynamics of dissociation. This, coupled with information on the early dynamics, gained perhaps through a study of the spectroscopy of the parent species, yields a significant body of data with which to develop and test theories of photodissociation dynamics. The use of spectroscopic techniques is prevalent in such studies of photodissociation, which require an intimate knowledge of the energy disposal between the various degrees of freedom [1]. Laser-induced fluorescence (LIF) and resonance enhanced multiphoton ionisation (REMPI) spectroscopy are most commonly used to determine the distribution over product internal energy states. Higher resolution studies of the polarisation dependence of single Doppler line profiles have further been instrumental in the determination of vector correlations for systems in which specific dynamical control is exhibited; hydrogen peroxide, H₂O₂, is a notable example [2,3]. Assum-

ing that the optically prepared excited state of the parent and the energy of the exciting radiation are known, then a measurement of the product translational velocities makes it possible to complete the energy balance in a photodissociation. The distribution of velocities also facilitates (and may be essential for) the inversion of line profile data to vector correlation information [4].

In a photodissociation which yields only two fragments a measurement of the centre-of-mass kinetic energy distribution, through energy conservation, determines the internal energy for the combined fragments. When the energy state of one of the fragments is known (e.g. an atom in its electronic ground state) or may be specified (e.g. a diatomic molecule described by the quantum numbers v'' and J''), the internal energy may be determined uniquely. In conventional time-of-flight mass-spectrometry (TOFMS) the kinetic energy distribution of mass-selected species is measured but, in general, the internal quantum states cannot be specified, and in this respect TOFMS has a limited applicability. Experiments which have combined REMPI and TOF techniques for the detection of atomic hydrogen have, however, proved fruitful, as H is the most sensitive monitor of the partner internal energy [5,6]. The

¹ Present address: Department of Chemistry, University of Toronto, Toronto, Canada M5S 1A1.

technique of velocity aligned Doppler spectroscopy (VADS) does offer the opportunity for quantum state specificity provided one of the fragments may be probed in LIF or REMPI. The opportunity arises here for the determination of the internal energy distribution in a "dark" partner, which might not otherwise be achieved by conventional methods. Furthermore, even when both fragments may be probed spectroscopically the measurement of vibrational distributions is often a difficult one to make directly, especially if contaminating species are present (as in the case of the nitrous acid system), and it may be preferable to obtain an indirect measurement from VADS.

Wittig and co-workers [7–10] have pioneered the VADS technique, measuring the recoil velocity distribution of photofragment H atoms from various precursors. Photolysis and probe lasers are counter-propagated coaxially through a low-pressure sample of gaseous precursor. By delaying the probe radiation following photolysis fragments with velocity components perpendicular to the probe wave vector escape from the probe region and avoid detection. For a narrow velocity distribution the Doppler profile of the Lyman- α line of the H photofragment, at long time delay, collapses to leave two outer wings, representing the speed along the probe direction. This, therefore, serves to separate the recoil velocity distribution from its angular distribution. It is necessary to use suitably collimated laser beams and work at sufficiently low pressures to ensure a collision-free environment over the time scale of the experiment. A structured Doppler profile obtained under these conditions directly reflects the population distribution of the partner, as demonstrated, quite elegantly, by the VADS line profile of H following photolysis of H₂S [9].

The resolution of this technique is limited by experimental factors, such as probe laser bandwidth and beam profiles, and by molecular factors including the parent thermal translational motion, the centre-of-mass recoil velocity distribution of the probed fragment and, of course, the internal energy distribution of the partner. Photofragment H is a particularly sensitive probe of the dynamics because, due to its small relative mass, it displays a correspondingly large Doppler shift. This has, for example, allowed the resolution of both spin-orbit states of Br in the photol-

ysis of HBr, using a conventional dye laser [9].

Photofragment OH following the photolysis of nitrous acid, HONO, in its electronically excited (\tilde{A}) state has recoil velocities an order of magnitude lower than those of atomic hydrogen [11,12] and the bandwidth of probe radiation generated by conventional pulsed dye laser systems becomes unacceptably large relative to the maximum Doppler shift in the line profile of a selected rovibronic transition. In this study of the VADS of OH from photolysis of HONO(\tilde{A}) this restriction is overcome by using a pulse-amplified continuous wave (cw) dye laser system, giving a linewidth of about 100 MHz in the ultraviolet (UV), thus providing a negligible contribution to the overall Doppler lineshape.

This report of the application of VADS to a diatomic fragment (namely OH) demonstrates the feasibility of the technique and suggests further application to other related photolysis systems, simple bimolecular reactions and to the determination of cross correlations between the quantum states of two molecular products. The latter has, in fact, recently been realised in a study of the photodissociation of H₂O₂ [13].

2. Doppler line profiles

We now consider in some detail the contributions to the observed Doppler line profile of a nascent photofragment, which may allow the determination of vector properties and the translational energy distribution.

2.1. Doppler shift

An absorbing photoproduct exhibits an apparent shift in resonant frequency by virtue of its velocity component along the direction of propagation of the analysing radiation. The distribution of velocity components along the probe (z direction) determines the detailed form of the spectral line profile. As Doppler shift is proportional to the parallel velocity then a spectral line profile which varies with probe wavelength (or reciprocal frequency, cm^{-1}) is simply a measure of the distribution of parallel velocity components. If we write $S(\bar{\nu})$ for the intensity as a function of frequency then

$$S(\bar{v}) \equiv S(u_z), \quad (1)$$

where $S(u_z)$ is the intensity as a function of velocity projection along the *laboratory* (probe laser propagation) axis z . There are many contributions to u_z arising from the speed and angular distributions in the recoiling fragments, from the dissociation, and the initial parent translational (thermal) distribution. These contributions will be considered below. The further contribution from the finite probe laser bandwidth is easily included, although the effect on the line shape of the pulse-amplified radiation is only minor.

2.2. Centre-of-mass (c.m.) recoil anisotropy, $R_z(v, v_z)$

The c.m. recoil distribution for a single velocity of recoil of a fragment produced by a linearly polarised photolysis source can be written in terms of the bipolar moments which describe the vector properties of dissociation [4]. In particular, for counter-propagated beams and perpendicular detection, we may express this angular distribution in terms of the velocity projections, v_z , along the direction of observation, as follows:

$$R_z(v, v_z) = [1 - \frac{1}{2}\beta P_2(v_z/v)]/2v, \quad (2)$$

where β is an effective anisotropy parameter and $P_2(v_z/v) = [3(v_z/v)^2 - 1]/2$ is a second-order Legendre polynomial. This function is merely the distribution of parallel velocity, v_z , derived from the angular distribution of the recoil velocity, $v = |v|$, from the photodissociation. In the limit of a single recoil speed, v , the Doppler profiles of spectral lines are directly related to R_z :

$$S(v_z) \equiv_{\text{single } v} R_z(v, v_z), \quad (3)$$

where $S(v_z)$ is the intensity as a function of *centre-of-mass* velocity projection arising from the dissociation.

2.3. Centre-of-mass velocity distribution $P(v)$

There is, in general, a spread in fragment velocity from the dissociation and in the VADS experiment the c.m. velocity distribution, $P(v)$, is the result we seek. The spread of internal energy in the recoiling

partner at fixed total available energy, $E_{\text{av}} = h\nu - D_0^0(\text{HO-NO})$, determines $P(v)$ by energy conservation. The recoil distribution, R_z is therefore weighted by the probability of finding a recoiling fragment with velocity, v . The resultant contribution to the line shape is given by

$$S(v_z) = \int_{|v_z|}^{\infty} P(v) R_z(v, v_z) dv, \quad (4)$$

where $v \geq v_z$ in order to allow a projection of v_z .

2.4. Parent (thermal) contributions, $T(u_q - v_q)$

The observed line shape represents the final distributions of velocity vectors along the probe direction, \hat{k}_a . The final velocity u is the vector sum of the c.m. fragment recoil velocity, v and the parent velocity, c :

$$u = c + v, \quad (5)$$

and the components of u and v in the direction \hat{k}_a are u_z and v_z , respectively. In the simple case of a single velocity, v , the line shape is a convolution of the parent molecule translational energy distribution in the z direction, $T(c_z) \equiv T(u_z - v_z)$, over the recoil anisotropy function $R_z(v, v_z)$, to yield the distribution in total projection, $S(u_z)$, given by

$$S(u_z) \equiv \int_{\text{single } v} \int_{-v}^v R_z(v, v_z) T(u_z - v_z) dv_z. \quad (6)$$

This is the summation over those pairs of values v_z and c_z which contribute to each value of u_z . If we now include a distribution of recoil velocity, $P(v)$, for the more general case we have

$$S(u_z) = \int_0^{\infty} P(v) \int_{-v}^v R_z(v, v_z) T(u_z - v_z) dv_z dv. \quad (7)$$

The distribution of parent translational energy in thermal equilibrium is given by a Gaussian of the form

$$T(u_q - v_q) = \frac{1}{u_0 \sqrt{\pi}} \exp\left[-\left(\frac{u_q - v_q}{u_0}\right)^2\right], \quad (8)$$

where $q = x, y$ or z and u_0 is a root mean square velocity of the distribution: $u_0 = (2kT/m)^{1/2}$.

2.5. Time delay and beam shapes: The VADS line profile, $Q(v-v_z)$

We have so far implicitly assumed that all recoiling fragments are detected with equal efficiency. The principle of the VADS experiment is that by using tightly collimated photolysis and probe beams and delaying the latter, fragments recoiling perpendicular to the probe direction, \hat{k}_a , escape from the interaction region and remain undetected. In an ensemble of parent molecules the production of a photofragment is dependent on the power density of photolysis radiation at the point in space of its birth, while the subsequent detection of this photofragment depends on the power density of the probe radiation at the point in space of its analysis. The separation of these two points in space is governed by the fragment velocity and the time delay between photolysis and probe pulses. We, therefore, require a knowledge of the beam profiles, as the intensity recorded at each u_z (i.e. \bar{v}) will be a function of the overlap, Φ , of the two beams. This type of analysis has been performed by Xu et al. [7,14], who simulated Lyman- α profiles of photofragment atomic hydrogen by numerical integration. We were able to develop an analytical treatment, based on their foundations, by assuming that both laser beams were uniform along their length (z direction) through the detection region and Gaussian in cross section. The power densities of such beams are a function of x and y only and vary with radial distance from the z axis, $r = (x^2 + y^2)^{1/2}$.

Consider photolysis at a point P and subsequent probing at a point Q, as shown in fig. 1. The spatial separation of P and Q is simply ut , where $u = |\mathbf{u}|$ is the laboratory velocity and t is the time delay between the lasers. The perpendicular separation of P and Q is $u_r t$, where u_r is the radial laboratory velocity. It is evident that as the time delay increases the vectors \mathbf{u} which terminate along the probe axis will have only a minor component, $u_r t$, perpendicular to z , and ultimately must also originate close to the probe axis. Therefore, with increasing time delay, observation of fragments is biased toward those which travel backwards or forwards along the probe laser axis. A reduction in beam waists will have the effect of discriminating in favour of those molecules with large parallel velocity components at a shorter time delay. Assuming cylindrical Gaussian beams with width pa-

rameters w_p , for the photolysis beam and w_a , for the probe beam, we find

$$\Phi(u, t) \equiv \Phi(u_x, u_y, t) = \exp\left(-\frac{2(u_x^2 + u_y^2)t^2}{w_p^2 + w_a^2}\right), \quad (9)$$

where $u_r^2 = u_x^2 + u_y^2$ and u_x and u_y are Cartesian components of the fragment velocity (\mathbf{u}) in the laboratory frame. As required, when the time delay $t=0$, all values of u_r give equal probability of detection and for $t>0$ we have a Gaussian function in u_r . This overlap function is the detection efficiency as a function of u_x , u_y and t , but each u_x and u_y has contributions from $c_x v_x$ and $c_y v_y$, respectively. Incorporating these contributions into eq. (7), the general expression for the line profile becomes

$$S(u_z) = \iiint P(v) R_z(v, v_z) \\ \times T(u_z - v_z) T(u_y - v_y) T(u_x - v_x) \\ \times \Phi(u_x, u_y, t) dv_x dv_y dv_z du_x du_y, \quad (10)$$

where the $T(u_q - v_q)$ are given in eq. (8). The terms in u_x and u_y can be integrated analytically and, with a change of variable, the expression for the probed axial distribution becomes simplified to

$$S(u_z) = \int_0^\infty P(v) \int_{-v}^v R_z(v, v_z) \\ \times T(u_z - v_z) Q(v - v_z) dv_z dv, \quad (11)$$

where

$$Q(v - v_z) = \frac{\omega^2 - u_0^2}{\omega^2} \exp\left(-\frac{v^2 - v_z^2}{\omega^2}\right), \quad (12)$$

and ω is given by

$$\omega^2 = \omega^2(t) = (w_p^2 + w_a^2)/2t^2 + u_0^2. \quad (13)$$

Hence, $Q(v - v_z)$ contains the sole dependence of the line profile on the beam diameters and the time delay between the two light pulses. This function is a truncated Gaussian with maxima at $v = v_z$ and maintains a finite width as $t \rightarrow \infty$, due to the parent thermal contribution, u_0 . It is also noteworthy that $Q(v - v_z)$ depends on the total cross-sectional beam waist area, which implies that the probe beam need not be the narrower beam – although this configuration is probably preferable for ease of alignment.

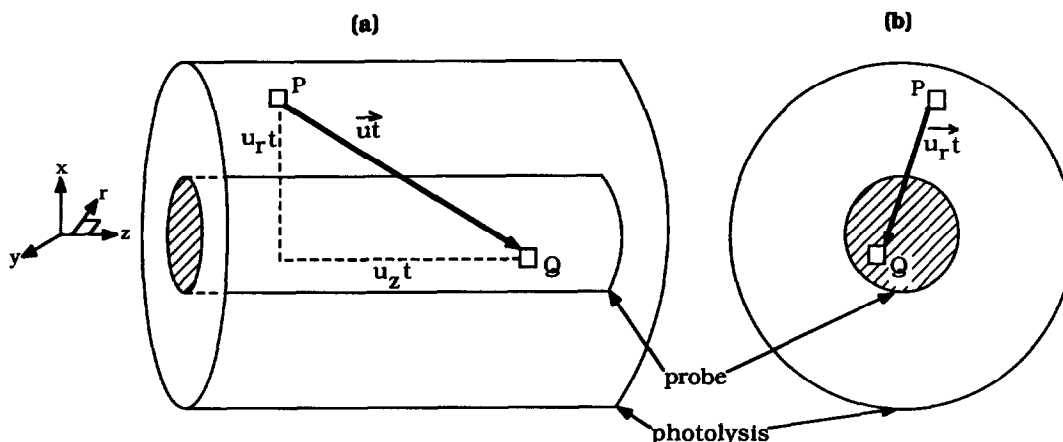


Fig. 1. A schematic of the VADS experiment, showing photolysis of the parent at point P and subsequent analysis of the fragment at point Q with coaxially aligned Gaussian laser beams. (a) Side view, (b) cross section.

Finally, the thermal convolution, $T(u_z - v_z)$, is independent of v and it is convenient, computationally, to perform this integration last. The general expression for the Doppler line profile recorded in a VADS experiment becomes

$$S(u_z) = \int_0^{\infty} G(v_z) T(u_z - v_z) dv_z, \quad (14)$$

where $G(v_z)$ contains the integration over v :

$$G(v_z) = \frac{\omega^2 - u_0^2}{\omega^2} \exp\left(\frac{v_z^2}{\omega^2}\right) \times \int_{v_z}^{\infty} P(v) R_z(v, v_z) \exp\left(-\frac{v^2}{\omega^2}\right) dv. \quad (15)$$

2.6. Line profile simulation

An illustrative example of a step-by-step simulation of the complete VADS line profile $S(u_z) \equiv S(\bar{v})$, for three different time delays between photolysis and analysis, is shown in fig. 2. In this example we take the translational energy distribution of OH, which is proportional to $P(v)/v$, to be that which is determined by the internal energy distribution of the NO partner, as found in our earlier, direct, study of this fragment [15]. In this experiment, the crude vibrational distribution measured was

$$N(v''=1) : N(v''=2) : N(v''=3) \approx 2 : 1 : 0.01, \quad (16)$$

while the rotational populations were well characterized by a Gaussian of the form,

$$N(J) \propto \exp\left[-4 \ln 2 \left(\frac{J - J_m}{J_w}\right)^2\right]. \quad (17)$$

The Gaussian parameters appropriate to the rotational population in each vibrational level were:

$$v''=1; \quad J_m=30, \quad J_w=15$$

and

$$v''=2; \quad J_m=26, \quad J_w=15. \quad (18)$$

The population in $v''=3$ was considered negligible and was omitted. Starting with an assumed recoil anisotropy function R_z (eq. (2)), with $\beta = -1$, and the velocity distribution, $P(v)$, consistent with the above internal energy distribution in the NO (inset in fig. 2), a convolution is performed to yield the profile F . Further convolution with the VADS detection efficiency profile Q (eq. (12)) for the three time delays, $t=100, 600$ and 1000 ns, results in the line shape G (eq. (15)). Final convolution with the parent thermal distribution, T (eq. (8)), yields the eventual line profile S (eq. (14)). For a short time delay the VADS function Q has very little effect on the final line shape, as expected, and S may be generated by direct con-

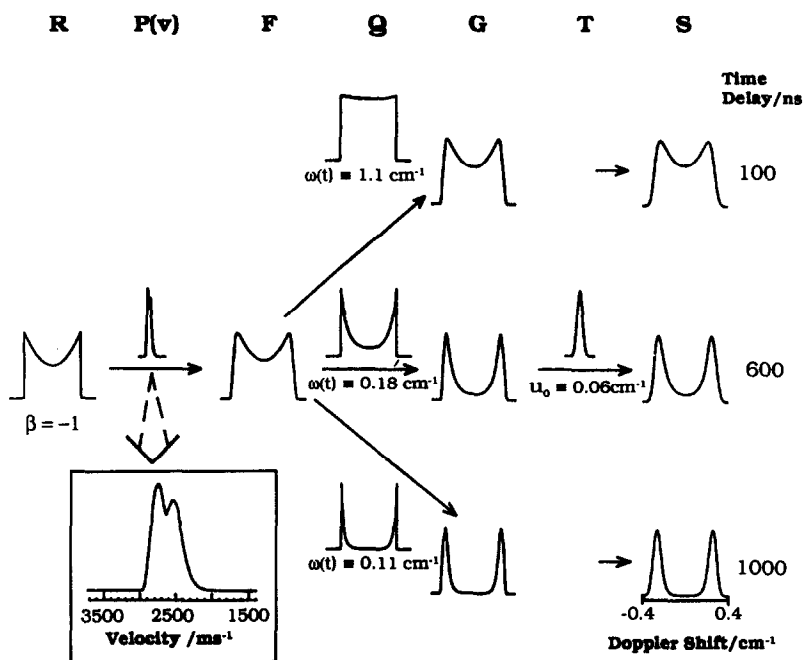


Fig. 2. Evolution of the VADS line profile $S(\bar{\nu})$ with increase in time delay from 100 to 1000 ns. The inset is an enlargement of the c.m. recoil velocity distribution. See text for details.

volution of F with T , such that the recoil anisotropy has a major influence. Conversely, at long time S reflects the velocity distribution, $P(v)$, and therefore the internal energy distribution of the partner.

The object of the Doppler line profile analysis is, in general, to obtain the velocity distribution, $P(v)$, and the effective recoil parameter, β . The simplest deconvolution of an experimental line profile follows from an accurate knowledge of the laser beam waists, w_p and w_a , allowing the expression $Q(u_z - v_z)$ to be generated for any desired time delay. A long time delay profile may then be simulated to give the best-fit velocity distribution, $P(v)$, and consequently, the energy distribution over the internal degrees of freedom in the partner. The determination of β follows from the best-fit simulation of a conventional Doppler line profile (short time delay and large beam waists), incorporating the, now determined, velocity distribution. A check of the reliability can be made by comparing line profiles taken at intermediate time delays with simulated profiles which embody these findings and vary only in their Q contribution, which contains the time dependence.

3. Experimental

A schematic of the experimental setup is shown in fig. 3. This configuration enabled the coaxial, counter-propagation of photolysis and narrow-band tunable probe radiation through a low-pressure sample of HONO, with a variable time delay between the two laser pulses. LIF from nascent OH was detected at right angles to both the laser beams and the axis along the sample input.

Two different photolysis wavelengths, at 355 or 369 nm, were used to dissociate HONO(\tilde{A}) in its 2^2 or 2^1 state, respectively, corresponding to excitations of the terminal N=O mode [16]. Radiation at 355 nm (< 5 mJ) was generated by frequency tripling in a Nd:YAG laser (JK Lasers HY-750), YAG1. Alternatively, in a separate experiment, light at 369 nm was produced by Raman shifting, in H_2 , the second harmonic output (532 nm) of YAG1. The second anti-Stokes (2AS) radiation was selected by angletuning a Pellin-Broca prism. The polarisation at the reaction chamber (horizontal, H_p , or vertical, V_p) was controlled by appropriate adjustment of the optical

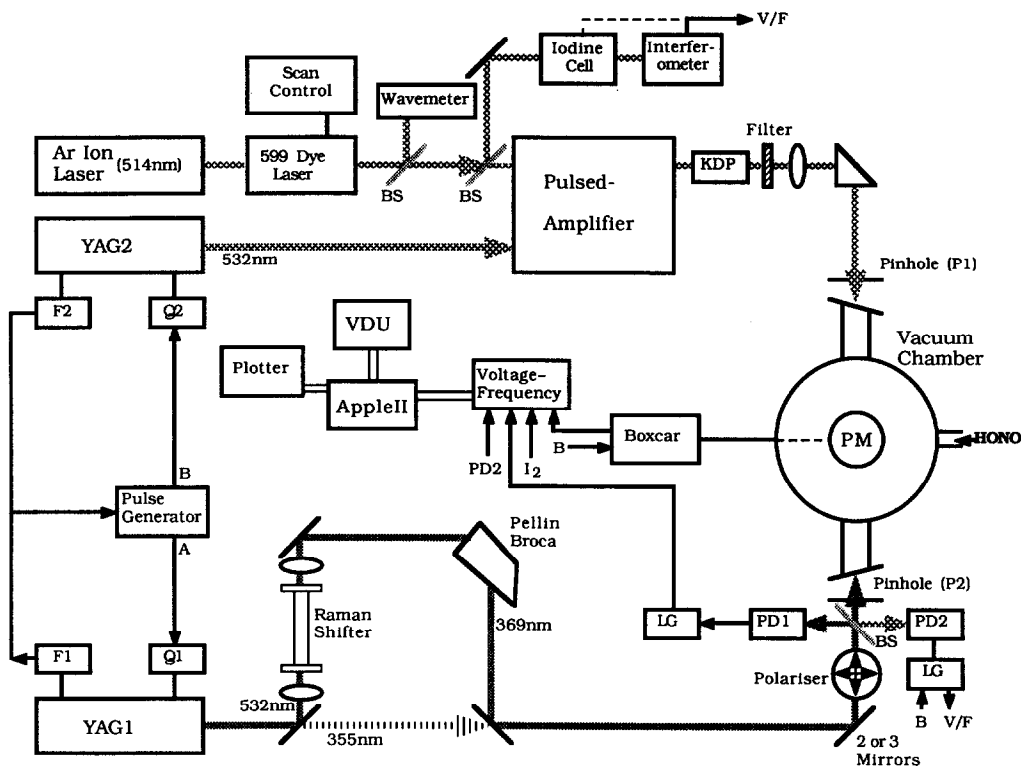


Fig. 3. Block diagram of the VADS experiment. A/B, trigger pulses; BS, beam splitter; F1/F2, YAG flashlamp controls; LG, linear gate; PD1/PD2, photodiodes; PM, photomultiplier; Q1/Q2, YAG Q-switch controls; V/F, voltage-to-frequency converter.

configuration and the use of a linear polariser (the results were polarisation independent).

Narrow bandwidth probe radiation of the required energy for excitation of OH in its $A^2\Sigma^+ \leftarrow X^2\Pi$ band around 308 nm was generated by frequency doubling in potassium dihydrogen phosphate (KDP) the output of a home-built pulse-amplified dye laser. This device combined the narrow linewidth of a cw laser with the high-power output of a pulsed laser to produce, after frequency doubling, radiation with a linewidth of ≈ 100 MHz (0.003 cm^{-1}) in the UV. A detailed discussion of the design and operation of the pulsed amplifier can be found elsewhere [17,18]. Briefly, three flowing dye cells were pumped by the 532 nm output of a second Nd:YAG laser (Spectron Laser Systems SL802), YAG2, as in a conventional dye laser. Frequency selection was provided by the

single-mode output of an argon-ion laser pumped dye laser (Coherent CR599-21), 599, as opposed to a diffraction grating. A solution of rhodamine 6G laser dye in ethylene glycol was circulated in the 599, while the pulsed amplifier was operated with solutions of sulphorhodamine 101 in ethanol. The oscillator and pre-amplifier stages were each side-pumped by about 10% of the light from YAG2 with the remaining portion end-pumping the final amplifier stage. The ratio of pulse-amplified radiation (PA) to amplified spontaneous emission (ASE) in the oscillator stage determined the overall performance of the pulsed amplifier. A high PA:ASE ratio was required for the optimum line shape and linewidth of probe radiation. The amplification stages slightly reduced the ratio but, generally, a ratio better than 4:1 was adequate and not too difficult to achieve. The pulsed

amplifier was able to produce about 1 mJ of pulsed light at the cw dye laser wavelength, which was subsequently doubled and filtered to give UV at the required probe wavelength. A linewidth of ≈ 100 MHz in the UV was measured from spectra of the hyperfine components of an electronic transition in atomic mercury [19]. The probe power was attenuated by adjusting the voltage supplied to the amplifier of YAG2 and using a 10% neutral density filter. Less than about 0.5 μ J of UV radiation was directed into the reaction chamber through a 2.5 m focal length quartz lens, and the linear polarisation of the beam was vertical (V_a). Even this rather low energy was sufficient to saturate the OH transitions, due to the narrow linewidth of the pulse-amplified light.

The stainless steel reaction chamber was of a typical vacuum can type; consisting of optical entrance and exit windows, baffles to reduce scattered light, fluorescence collection optics and a port to admit the gas sample. Evacuation was by use of an oil diffusion pump (8" diameter) and a rotary backing pump. The HONO sample was prepared as described previously [15], by addition of acid to sodium nitrite and admitted continuously to a point ≈ 1 cm from the interaction region through a crude nozzle. The sample was simply exhausted through the nozzle (≈ 1.5 mm diameter pinhole) resulting in a partially collimated flow. Entrance and exit pinholes (P1 and P2) served to adjust the laser beam diameter and to render the two beams parallel through the interaction region.

Absolute calibration of the probe frequency was provided by recording the LIF excitation spectrum of molecular iodine, excited by a portion of the cw light, while accurate relative calibration was achieved by monitoring the transmission fringes of a 0.0156 cm^{-1} confocal interferometer. The maximum scan width of the 599 was only 30 GHz in the visible or about 2 cm^{-1} in the UV, therefore, few I_2 transitions were observed in each scan, making it difficult to determine the absolute wavelength. A home-built wavemeter, in which the wavelength of the 599 was compared to the standard of a He-Ne laser ($\lambda = 632.8173\text{ nm}$ in air), greatly facilitated the selection of the appropriate 599 scan encompassing the desired wavelength region.

The time delay between photolysis and probe beams in the interaction region of the vacuum chamber was made continuously variable in the range 0–2000 ns by using a pulse generator (Pulsetek) to di-

rectly activate the Q switches of YAG1 and YAG2, separated by a serial delay. The flashlamp trigger of YAG1 (10 Hz repetition rate) synchronously activated the flash lamps of YAG2, triggered the pulse generator and initiated data collection from the photodiode monitoring the photolysis power (PD1). The first pulse from the pulse generator fired YAG1 following an optimum delay of $\approx 200\ \mu\text{s}$, while the second pulse fired YAG2 following a similar, though variable, delay. An adjustment of less than about 5 μs in this delay did not affect the laser output or result in "pre-lasing" and provided the required timing for the experiment. The firing of YAG2 also initiated data collection of probe power (via PD2) and any LIF in the reaction chamber. In order to accurately set the time delay, both beams were scattered onto the face of a UV sensitive photodiode positioned near the reaction chamber and its response observed on a 100 MHz oscilloscope. The adjustment of the serial delay of the pulse generator gave the desired time delay with a jitter of less than $\approx 2\text{ ns}$.

OH fluorescence was imaged into a blue sensitive photomultiplier (EMI 9824-QB), through an OH line filter (Ealing 35-8044), which gave $\approx 15\%$ transmission at $310 \pm 12\text{ nm}$. The recording of scattered light from the photolysis at short delays was avoided by suitable electronic gating. Four channels of data were collected via a voltage-to-frequency converter and stored on an Apple II microcomputer. LIF signal, both probe and photolysis powers and either I_2 lines or etalon fringes were recorded.

All the results discussed below were taken by monitoring the line profile of the OH($A\ ^2\Sigma^+, v' = 0 \leftarrow X\ ^2\Pi, v'' = 0$) $P_1(2)$ transition, but the experimental procedure adopted was equally applicable to any transition. The OH(0–0) frequencies of Dieke and Crosswhite [20] were used to calculate the corresponding wavemeter reading and the appropriate 599 scan was selected accordingly. Verification that the desired wavelength had been selected was achieved by recording the I_2 transitions in this region (at the undoubled frequency) followed by comparison with the documented spectrum [21]. The $P_1(2)$ line was centred within a 17 GHz scan of the 599 dye laser (equivalent to $\approx 1\text{ cm}^{-1}$ at the UV wavelength) and the line profile of the nascent OH was recorded synchronously with etalon transmission fringes and both laser powers over about 1800 data points. The line

profile was recorded with increasing time delay between the pump and probe lasers until no further increase in spectral definition was attained. The time scale of the experiment was determined by the profiles of the photolysis and probe beams and the number density in the interaction region. Experience determined that the approximate diameter of the photolysis pinhole, P1 was ≈ 1.5 mm, although the beam was slightly diverging, while that of the probe pinhole P2 was ≈ 1 mm. The probe diameter was actually less than this due to the focusing effect of the $f=2.5$ m lens. The continuous nozzle was adopted in order to reduce the local density of the gaseous sample; an effusive source was found to result in "thermalisation" of photofragments by collision. Under these conditions of beam diameter and local pressure, LIF from nascent OH could be observed in a "collision-free" environment over a period of $1.5 \mu\text{s}$, although no further spectral definition was observed for time delays greater than $1 \mu\text{s}$.

4. Results

Presented in fig. 4 are time delayed Doppler profiles of the $P_1(2)$ line of OH following the photolysis of HONO(\tilde{A} , 2^2) at 355 nm. The experimental profiles, as expected, show an improved spectral definition with increasing time delay. The change in the profiles is quite dramatic and is a consequence of the fact that the width of the angular distribution of the recoiling OH sampled by the probe becomes smaller. The calculated profiles include the contributions described in section 2, and these are compared with the experimental profiles. Unfortunately, the analysis was complicated by our limited knowledge of the beam waists, w_p and w_a , as these were difficult to measure. In view of this, we incorporated $\omega(t)$ (eq. (13)) as a variable parameter in the simulation of an intermediate time delay profile ($t=600$ ns), where we expected little dependence on the form of $P(v)$ (see fig. 2). A best fit value of $(w_p^2 + w_a^2)^{1/2} = 1.1$ mm was determined and then held constant in subsequent calculations of $\omega(t)$, for the remaining simulations. Assuming a single recoil velocity, a conventional short-time, large beam waist Doppler profile was fitted to obtain a value of the effective recoil anisotropy parameter β . Given this value of β and the value of

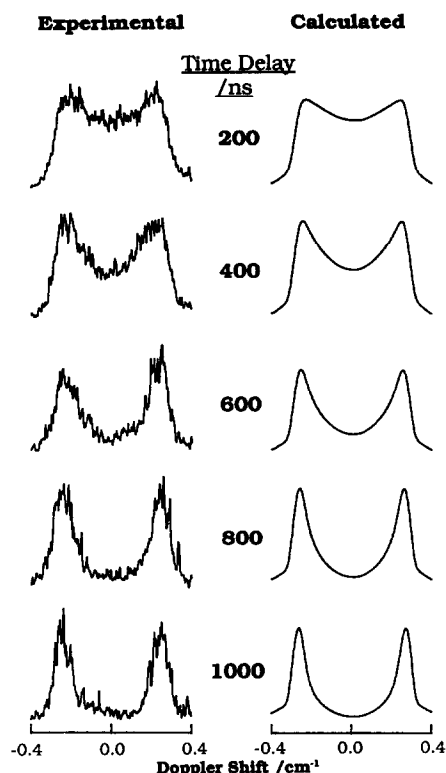


Fig. 4. VADS profiles of the $P_1(2)$ line of nascent OH following photolysis of HONO(2^2). The centre frequency is 39390.94 cm^{-1} and is that of OH at rest.

$\omega(t=1000 \text{ ns})$, the long-time (1000 ns) profile was simulated to find the best form of $P(v)$. The short-time, large beam waist profile was resimulated with $P(v)$ fixed to obtain a final value for β . The intermediate time delay profiles provided a check of the consistency of β , $P(v)$ and $\omega(t)$, as only the value of the time delay, t , was changed in each case.

The above procedure was not, however, completely satisfactory. It was found that the effective spectral width of the parent thermal distribution was less than that anticipated for a room temperature distribution along the z axis, due to the collimating effect of the continuous nozzle source. A Gaussian width of about 0.03 cm^{-1} was used in the simulations to account for this, while a value of $u_0 \approx 0.06 \text{ cm}^{-1}$ (full parent width) was still applicable to the distributions along x and y – which enter into the function Q (eq. (12)). The effect of the laser line

shape was investigated by recording the line profiles of OH produced in the reaction of NO₂ with H atoms (generated by a microwave discharge through H₂O vapour). OH generated in this way is thermally equilibrated by multiple collisions and has a calculated Doppler width of $\approx 0.10 \text{ cm}^{-1}$. The observed width was not perceptibly different indicating the negligible contribution made by the laser bandwidth. However, an apparent “tail” to these profiles was observed, and was the result of a broad Gaussian ASE base to the laser profile. This type of effect is common in experiments involving pulse-amplified, frequency-doubled radiation [22] and is due to the combination of off-centre lasing frequencies with those in the centre. Modelling of the thermal OH profiles lead to an estimated Gaussian base of about 0.25 cm^{-1} in width and a ratio of central Gaussian laser spike to ASE background of ≈ 9 . This effect was incorporated into the calculated profiles shown in fig. 4.

The velocity distribution, $P(v)$, in the simulations, in fact corresponds to the rotational distributions and approximate vibrational distribution found from the direct measurements on the NO partner (eqs. (16)–(18)). This vibrational distribution was required to satisfactorily fit the outer edges of the short-time, large beam waist (no pinholes or focusing lenses) profiles. In these profiles the contribution to the wings comes from the high-velocity components along the z axis and corresponds to a lower internal energy in the partner NO. There was apparently not a significant contribution from NO in $v''=0$, in which by extrapolation we would expect a rotational distribution peaked at high J with a similar spread to that observed in $v''=2$ and 3 ($J_m=34$, $J_w=15$, for example). A significant population in $v''=1$ was, however, required to fit these short-time spectra. The actual form of the internal energy distribution is difficult to realise by deconvolution of the VADS profiles because the peak value of J in the rotational distributions decreases with increasing vibrational quanta and fortuitously the distributions overlap considerably in total energy. The effect of this fairly narrow internal energy distribution in the NO is to produce a narrow range of OH recoil velocities, $P(v)$, which consequently has little influence on the derived value of β . The best-fit value of $\beta \approx -0.75$ is, therefore, very close to that obtained in an earlier study of the OH, of $\beta \approx -0.8$ [12]. We conclude only, that the estimated

internal energy distribution obtained in the direct study of NO [15] is consistent with that required to fit the VADS profiles of the partner OH.

The calculated and experimentally observed profiles are in fairly good, but not perfect, agreement. We note that the full-width of the experimental profiles remains almost constant while the central contrast increases at longer time, whereas the full-width of the calculated profiles increases slightly. The latter is to be expected, because as the time delay increases the simulation becomes more like the convolution of the parent thermal distribution with a delta function positioned at the maximum Doppler shift. Hence, for a “top-hat” recoil function ($\beta=0$) the full Doppler width increases by an amount equal to the parent thermal width (plus laser contribution, if significant) between zero and infinite time delay. The observed trend in full-widths may be due to a non-Gaussian nature of the photolysis beam which is likely to have been diffracted through the input pinhole and was also slightly diverging. The widths of the wings in the long-time profiles did not narrow significantly for $t > 800 \text{ ns}$ in contrast to the calculated profiles and consequently the long-time simulations do not fit perfectly.

An example of the calculated and best-fit profiles in the $t=1000 \text{ ns}$ profile is shown in fig. 5. The calculated profile has a value of $\omega(t) \equiv 0.12 \text{ cm}^{-1}$ according to the procedure outlined above, while the best-fit profile was that obtained by floating the value

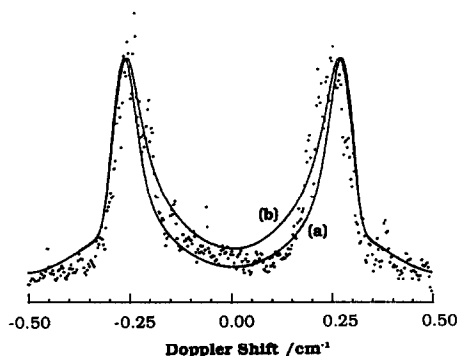


Fig. 5. Calculated and best-fit profiles for the $t=1000 \text{ ns}$ line profile of $P_1(2)$ following photolysis at 355 nm, (a) $\omega(t) \equiv 0.12 \text{ cm}^{-1}$ ($((w_p^2 + w_d^2)^{1/2} = 1.1 \text{ mm})$), (b) $\omega(t) \equiv 0.155 \text{ cm}^{-1}$ ($((w_p^2 + w_d^2)^{1/2} = 1.4 \text{ mm})$), respectively. The centre frequency is 32390.94 cm^{-1} . The dots are experimental data points.

of $\omega(t)$: the convergent value was $\omega(t) \equiv 0.155 \text{ cm}^{-1}$. The rather larger than expected limiting width to the wings in the experimental profile may be due to the effects of collisions. As the time delay increases the probability of collisions is greater, especially for the faster moving molecules, and we might expect molecules that would have contributed to the outer edge of the profile under collision-free conditions will contribute instead to the middle. We envisage that this would not only serve to broaden the outer wings but also reduce the overall Doppler width. Saturation effects may also play a role in broadening the wings. Due to the very narrow linewidth of the pulse-amplified radiation the power per unit bandwidth is high, such that small fractions of a microjoule of energy are sufficient to saturate those transitions which have a strong transition probability. This is particularly important in comparison of different transitions but may also affect the intensity across a single line profile. In particular, within any one Doppler profile all the molecules will saturate in the same way, but a small symmetrical broadening will be added to the peaks.

One further possible contributing effect that we consider is that of molecular flow from the continuous nozzle. If the forward flow of the HONO molecules is significant then at longer time delay there will be an increasing contribution to the line profile made by molecules recoiling off-axis in the c.m. frame, in particular from those with low recoil speeds. This would also serve to broaden the wings. Although the conditions of flow have not been characterised, given an estimate of the backing pressure (≈ 20 Torr) and the wide pinhole (≈ 1.5 mm diameter), the resultant broadening is not expected to be appreciable. We should note that a collimated (not necessarily cooled) source of parent molecules is desirable in order to minimise the component of parent velocity, c_z , along the probe axis. In principle it should be possible to improve the experimental resolution until it becomes limited by the laser linewidth (0.003 cm^{-1} in our case). In such a case an allowance for forward flow can be made in the line profile simulations themselves or the probe and photolysis laser axes may be offset at each time delay to account for the mean flow velocity.

A detailed analysis of the OH Doppler line profiles obtained in the dissociation of HONO(\bar{A} , 2^1) at 369 nm was not undertaken due to the poorer quality of

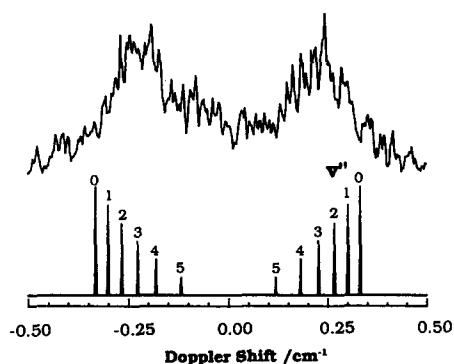


Fig. 6. The line profile of the OH $P_1(2)$ transition following photolysis of HONO(2^1) at 369 nm. Beneath are the positions of the maximum Doppler shifts corresponding to the lowest rotational levels in $v'' = 0-5$ of the NO partner. The centre frequency is 32390.94 cm^{-1} .

the data. We did observe, however, that the central contrast in these profiles was not as marked as in the dissociation of HONO(2^2), which seems to imply a rather wider internal energy distribution in the NO partner produced by the 2^1 dissociation. Unfortunately, in this case we have no data, obtained in a direct study of the photodissociation at this wavelength, with which to compare. Fig. 6 shows a representative $t = 1000$ ns VADS line profile of the $P_1(2)$ transition of OH following photolysis of HONO(2^1). Plotted beneath are the maximum Doppler shifts which, by energy conservation, correspond to the lowest rotational levels in $v'' = 0-5$ of the NO partner. The peaks are for reference purposes only and are not intended to represent a match to structure in the experimental spectrum. Given this reference, if we assume an inverted rotational distribution similar to that observed for the HONO(2^2) dissociation; the NO internal energy distribution for the HONO(2^1) dissociation appears to peak in $v'' = 1$ or 2 but $v'' = 0$ is not apparently significantly populated, unless at extremely high J .

5. Discussion

5.1. Photodissociation dynamics of HONO(\bar{A})

We have been unable to determine accurately the full vibrational distribution in nascent NO following

dissociation of HONO(2^n , $n=1$ and 2). Nevertheless we are able to conclude that the vibrational energy in the NO fragment from the 355 nm photolysis of HONO(2^2) is distributed mainly in $v''=1$ and 2 . The overlap in total energy, due to the degree of rotational excitation in each v'' , results in a narrow internal energy distribution overall ($\approx 1700 \text{ cm}^{-1}$ in width), which is reflected in the VADS profiles of the partner OH. The consistency between these results and those from a direct study of the NO [15] is encouraging, for it unequivocally identifies the parentage of the NO in the direct experiments as HONO. Measurements of NO($v''=2$ and 3) Doppler broadened linewidths in the earlier work were also used to conclude the identity of the parent. An accurate measurement of the vibrational distribution was, however, hampered by the presence of other NO precursors which produced NO predominantly in $v''=0$ and 1 . The NO internal energy distribution following dissociation of the 2^1 state is poorly resolved in the VADS profile of OH, but we are able to conclude that there is apparently a lack of significant population in $v''=0$ of the NO partner, unless the rotational distribution in this vibrational state is very highly inverted ($J \gtrsim 40.5$). It is clear from this work that studies of systems with a chemical and photochemical complexity akin to that of the HONO equilibrium [23] are able to benefit from VADS measurements of fragments which have a unique parentage.

The observed translational energy release, rotational-translational energy partitioning and anisotropic velocity and angular momentum distributions are testimony to the impulsive nature of the HONO dissociation [12,15]. We anticipate that the dissociative HONO(\tilde{A}) potential energy surface is bound in the terminal N=O coordinate, $r(\text{NO})$, but sufficiently repulsive along the coordinate parallel to the breaking O-N bond, $R(\text{ON})$, that dissociation is fast compared with torsional or rotational motions. A Franck-Condon treatment of photodissociation has been found to adequately model a number of other systems, such as H₂O(\tilde{A}) [24], which display similar evidence of prompt dissociation as that seen for the HONO dissociation. However, our observations do not concur with the calculations of the NO vibrational distributions by Vasudev et al. [12] which were based on a modified Franck-Condon model of the dissociation. For dissociation of HONO(2^n , $n=0-3$)

these predict a wide distribution in NO(v'') and for $n \geq 1$ the distributions are bimodal, peaking at $v''=0$ and again at $v'' > n$. The assumptions of prompt dissociation with no exit-channel interactions, which underlie this model, are evidently not appropriate in this case.

It is apparent that exit-channel interactions do play a role in determining the vibrational state distributions and we might expect that the degree of vibrational adiabaticity be sensitive to the detailed form of the HONO(\tilde{A}) potential energy surface. Detailed experimental and theoretical studies, based on an ab initio potential energy surface, of the photodissociation of the related CH₃ONO(S_1) are available for comparison. The characteristics of the CH₃ONO(S_1) dissociation are somewhat similar to those of HONO(\tilde{A}); due primarily to the fact that the $\pi^* \leftarrow n$ excitation [25,16] and subsequent bond rupture are centred on the planar R-O-N=O moiety [26,27]. The NO fragments, in both cases, are ejected predominantly in the plane with a high degree of rotational excitation, which is adequately parameterised by a Gaussian function in rotational quantum number [28,15]. Ab initio calculations show that the excited state potential energy surface of HONO(\tilde{A}) resembles that of CH₃ONO(S_1) in the $r(\text{NO})$ and $R(\text{ON})$ coordinates [29], so that we expect to observe a similar influence on the vibrational distribution in the NO. The fragment distributions from photolysis of CH₃ONO(3^n , $n=1-5$) are observed to occupy primarily NO($v''=n-1$) [30]. A dynamical calculation based on an ab initio surface of CH₃ONO(S_1) by Nonella and Huber [31] is able to satisfactorily model the observed results [32]. The S_1 surface is bound in the $r(\text{NO})$ coordinate and has a shallow well near the Franck-Condon region (accessed by a "vertical" electronic transition from the ground state). Perhaps more enlightening, as far as the dynamics are concerned, is the form of the vibrationally adiabatic potentials generated from this surface by retaining the nodal integrity of the $r(\text{NO})$ dependence of the vibrational wavefunction and calculating the corresponding energy as a function of $R(\text{ON})$. The resulting curves have a low barrier to dissociation along $R(\text{ON})$ in the Franck-Condon region and, due to the shortening of the N=O bond length and increasing vibrational spacing as $R(\text{ON})$ increases, this effective barrier increases with the number of quanta initially

excited. The competition between adiabatic (tunneling) and non-adiabatic (intramolecular vibrational relaxation, IVR) ultimately determines the final state distribution. The effective barrier in this case is such that the predominant process is vibrationally non-adiabatic dissociation. Unfortunately, no experimental observations were made of the vibrational distribution following photodissociation of $\text{CH}_3\text{ONO}(3^0)$ in which the adiabatic channel should dominate.

Completely analogous dynamical calculations on an ab initio potential surface of $\text{HONO}(S_1 \equiv \tilde{A})$ [29] are now available for direct comparison with our experimental findings. The theoretical analysis predicts that HONO dissociates in the same general way as $\text{CH}_3\text{ONO}(S_1)$. In particular, the effective barrier to dissociation in the $R(\text{ON})$ coordinate is approximately twice that found for CH_3ONO (the ONO bond angles in each case were fixed at their respective ground state values), favouring the vibrationally non-adiabatic dissociation channel. The dominance of the non-adiabatic route was heightened by increasing the strength of vibrational–translational (V–T) coupling in the exit channel, and was required in order to improve the comparison between the calculated and experimental absorption spectra. Consequently, the predicted distributions over $\text{NO}(v'')$ arising from dissociation of $\text{HONO}(2^n, n=0, 1, \dots)$ were found to peak at $v''=0$ for $n=0$ and 1, irrespective of the degree of V–T coupling, while $\text{NO}(v''=n-1)$ and $\text{NO}(v''=n-2)$ were most populated for $n \geq 2$ when V–T coupling was weak and strong, respectively. In all coupling cases $\text{NO}(v'' > n)$ was virtually unexcited. In the experimental photodissociation of $\text{HONO}(2^n, n=1, 2)$ we do observe NO chiefly in $v''=1$ resulting from $\text{HONO}(2^2)$, consistent with a vibrationally non-adiabatic mechanism, but do not observe a significant population in $v''=0$ in the $\text{HONO}(2^1)$ dissociation. In the $\text{HONO}(2^2)$ case the presence of a significant population in $\text{NO}(v''=3)$ was observed in an earlier experiment, in which the NO was probed directly using laser-induced fluorescence [15], and the VADS line profiles presented in this paper of OH from both the $\text{HONO}(2^1)$ and $\text{HONO}(2^2)$ dissociations certainly indicate that $\text{NO}(v'' > n)$ is produced. Experimentally, therefore, dissociation preceded by vibrational relaxation in the

exit channel is less favoured than predicted theoretically.

The experimental observations may be rationalised if the effective barriers to dissociation along $R(\text{ON})$ in the case of $\text{HONO}(\tilde{A})$ were lower than those calculated for $\text{CH}_3\text{ONO}(S_1)$, and were in fact to become rather flat along $R(\text{ON})$ in the Franck–Condon region for the lowest states of the vibrational manifold. In this scenario, the adiabatic pathway dominates for the lowest values of the vibrational quantum number, n , of the parent (increasing the relative yield of $\text{NO}(v'' > n)$ perhaps), while at higher n the non-adiabatic channel dominates. Furthermore, an increasing energy separation between the vibrationally adiabatic curves as n increases would reduce the extent of vibrational–translational coupling and may be responsible for the reduced rate of dissociation indicated by a sharpening of vibrational structure in the parent absorption spectrum [16]. Given that OH has a substantially lower mass than CH_3O we anticipate that the $\text{HONO}(S_1)$ surface is a more sensitive function of the ONO bond angle and that, as preliminary ab initio calculations show [29], with the inclusion of this coordinate the relative barrier height along the dissociation coordinate is in fact lower than for the fixed angle calculation.

Clearly, a more comprehensive experimental study of the vibrational distribution for a wide range of initial parent vibrational excitation in parallel with dynamical calculations will be required before we can draw firmer conclusions about the form of the \tilde{A} state potential energy surface of HONO. Velocity aligned Doppler spectroscopy will, however, be a valuable addition to our armoury of diagnostics in subsequent investigations.

5.2. The VADS technique

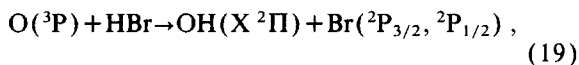
The feasibility of velocity aligned Doppler spectroscopy of photofragment diatomic molecules has been demonstrated. The VADS profiles of OH from the dissociation of $\text{HONO}(\tilde{A})$ have not proved to be particularly revealing of the partner NO internal energy distribution because, as mentioned above, the mean rotational energy in each vibrational state is a considerable fraction of the vibrational separation resulting in a significant overlap in total energy. This pilot study does, however, prompt suggestions for

improvement of these measurements. The major limitation to the resolution in the long time delay spectra is due to the thermal distribution in parent translation. If a molecular beam source was employed and crossed at right angles by the laser beams then any parallel component along the probe direction from parent molecules would be minimised. In principle, the energy resolution would be limited by the laser bandwidth (≈ 100 MHz in the UV with our pulse-amplifier system). It is not necessary to rotationally cool the parent, although this may also be desirable (this causes the nature of the parent species to change in the HONO experiment! [23]), but to ensure that the molecular flow is well collimated – by using closely packed narrow bore capillaries or a rectangular slit, for example. The analysis of the VADS line profiles would also be facilitated by a more accurate knowledge of the profiles of the photolysis and analysis laser beams, so that the velocity distribution, $P(v)$, and the effective recoil parameter, β , can be determined routinely.

VADS will, in general, be a useful diagnostic when there is a narrow internal energy distribution in a heavy recoiling partner, such that differences in the partner internal energy have a large effect on the translational recoil energy of the probed fragment. A further interesting possibility, not explored in this work, is the application of VADS to the investigation of correlations between internal energy states of photofragments. A coincidence experiment such as this would be impractical in the HONO dissociation due to the high density of states available. An experiment of this sort does become viable for systems in which one of the fragments has few but well separated internal energy states. An atomic fragment such as halogen, for example, exhibits spin-orbit coupling resulting in two well separated, but often accessible, electronic states. In a recent study of the photodissociation of NOBr [33] the existence of Br in both of its spin-orbit states, $^2P_{3/2}$ and $^2P_{1/2}$, was inferred from the fits of NO Doppler line profiles, which required the inclusion of two discrete translational energies to simulate the experimental data. The application of VADS to this system would allow the resolution of these two reaction channels, which are separated by a spin-orbit splitting energy of 3685 cm^{-1} [34], provided that a sufficiently narrow laser bandwidth can be achieved at the probe wavelength. Inter-fragment

correlations could also be investigated by varying the probed transition.

A similar prospect arises for interrogating a pair of molecular/atomic products from a simple chemical reaction. Consider the bimolecular reaction:



if the collision energy of the reactants can be defined then the production of both spin-orbit states of Br may be resolvable in the VADS profile of the partner OH. In a recent experimental study of this system [35,36] O(^3P) was generated by the 355 nm photolysis of NO_2 , with a spread in translational energy determined by the internal energy distribution in the NO partner. The energy available for partitioning between O(^3P) and NO($\text{X } ^2\Pi$) is about 3000 cm^{-1} and, based on results obtained in the 337 nm photolysis of NO_2 [37], is expected to be widely distributed over the NO internal energy states. An anomaly in the observed OH($v'' = 1$) distribution seemed to imply the opening of the reaction channel leading to OH + Br($^2\text{P}_{1/2}$). We note that at the threshold for production of the higher energy $^2\text{P}_{1/2}$ state, the difference in Doppler shifts for a transition in the OH($\text{A } ^2\Sigma^+, v' = 1 \leftarrow \text{X } ^2\Pi, v'' = 1$) band will be about 0.24 cm^{-1} . This should easily be resolved in the VADS profiles of the OH despite the distribution in collision energy, allowing measurement of the spin-orbit branching ratio in the Br partner, provided that care is taken to minimise the delay between production of the O atom precursor and the subsequent reactive collision. VADS profiles of different OH transitions may allow a correlation to be made between the spin-orbit states of the Br and the rotational states of the OH.

There are undoubtedly other systems for which VADS may yield valuable information regarding energy partitioning or inter-fragment correlations. The wider application of this technique is certain to enhance future investigations of photodissociation and reaction dynamics.

6. Conclusion

We have demonstrated the potential of velocity aligned Doppler spectroscopy as a probe of the en-

ergy distribution of molecular fragments born from photodissociation or chemical reaction. We believe that the amount of information attainable with this technique will be maximised by employing collimated beams of molecules in conjunction with high-resolution sources of probe radiation.

The photodissociation of trans-nitrous acid from its first electronically excited state occurs rapidly in the plane of the parent molecule to yield fragment NO with a distribution over vibrational states. Direct probing of the vibrational distribution and the use of VADS reveal evidence of both vibrationally adiabatic (tunneling) and non-adiabatic (IVR) dissociation channels. The observations indicate a dissociation which is less extreme than predicted by dynamical calculations on a model potential energy surface, based on a fixed ONO angle geometry, in which intramolecular vibrational relaxation was found to dominate.

Acknowledgement

We gratefully acknowledge the financial support of the Science and Engineering Research Council which made this work possible. We also thank C.M. Western and K.N. Rosser for their computational and technical expertise.

References

- [1] M.N.R. Ashfold and J.E. Baggott, eds., *Molecular Photodissociation Dynamics* (Royal Society of Chemistry, London, 1987).
- [2] K.-H. Gericke, S. Klee, F.J. Comes and R.N. Dixon, *J. Chem. Phys.* 85 (1986) 4463.
- [3] M.P. Docker, A. Hodgson and J.P. Simons, *Faraday Discussions Chem. Soc.* 82 (1986) 25.
- [4] R.N. Dixon, *J. Chem. Phys.* 85 (1986) 1866.
- [5] H.J. Krautwald, L. Schnieder, K.H. Welge and M.N.R. Ashfold, *Faraday Discussions Chem. Soc.* 82 (1986) 99.
- [6] J. Biesner, L. Schneider, G. Ahlers, X. Xie, K.H. Welge, M.N.R. Ashfold and R.N. Dixon, *J. Chem. Phys.* 88 (1988) 3607.
- [7] Z. Xu, B. Koplitz, S. Buelow, D. Baugh and C. Wittig, *Chem. Phys. Letters* 127 (1986) 534.
- [8] B. Koplitz, Z. Xu, D. Baugh, S. Buelow, D. Hausler, J. Rice, H. Reisler, C.X.W. Qian, M. Noble and C. Wittig, *Faraday Discussions Chem. Soc.* 82 (1986) 125.
- [9] Z. Xu, B. Koplitz and C. Wittig, *J. Chem. Phys.* 87 (1987) 1062.
- [10] B. Koplitz, Z. Xu and C. Wittig, *Chem. Phys. Letters* 137 (1987) 505.
- [11] R. Vasudev, R.N. Zare and R.N. Dixon, *Chem. Phys. Letters* 96 (1983) 399.
- [12] R. Vasudev, R.N. Zare and R.N. Dixon, *J. Chem. Phys.* 80 (1984) 4863.
- [13] R.N. Dixon, J. Nightingale, C.M. Western and X. Yang, *Chem. Phys. Letters* 151 (1988) 328.
- [14] Z. Xu, B. Koplitz and C. Wittig, *J. Chem. Phys.* 90 (1989) 2692.
- [15] R.N. Dixon and H. Rieley, *J. Chem. Phys.* 91 (1989) 2308.
- [16] G.W. King and D. Moule, *Can. J. Chem.* 40 (1962) 2057.
- [17] K.N. Rosser, M.Sc. Thesis, University of Bristol, UK (1986).
- [18] M.N.R. Ashfold, R.N. Dixon, K.N. Rosser, R.J. Stickland and C.M. Western, *Chem. Phys. Letters* 101 (1986) 467.
- [19] N. Little, Ph.D. Thesis, University of Bristol, UK (1988).
- [20] G.H. Dieke and H.M. Crosswhite, *J. Quant. Spectry. Radiative Transfer* 2 (1962) 97.
- [21] S. Gerkenstorn and P. Luc, *Atlas du Spectre D'Absorption de la Molecule d'Iode* (CNRS, Paris, 1978).
- [22] G. Bollen, H.J. Kluge, K. Wallmeroth, H. Schaff and R.B. Moore, *J. Opt. Soc. Am. B* 4 (1987) 329.
- [23] H. Rieley, Ph.D. Thesis, University of Bristol, UK (1988).
- [24] D. Hausler, P. Andresen and R. Schinke, *J. Chem. Phys.* 87 (1987) 3949.
- [25] P. Tarte, *J. Chem. Phys.* 20 (1952) 1570.
- [26] P.H. Turner, M.J. Corkill and A.P. Cox, *J. Phys. Chem.* 83 (1979) 1473.
- [27] A.P. Cox, A.H. Brittain and D.J. Finnigan, *Trans. Faraday Soc.* 67 (1971) 2179.
- [28] U. Brühlmann, M. Dubs and J.R. Huber, *J. Chem. Phys.* 86 (1987) 1249.
- [29] S. Hennig, A. Untch, R. Schinke, M. Nonella and J.R. Huber, *Chem. Phys.* 129 (1989) 93.
- [30] O. Benoist D'Azy, F. Lahmani, C. Lardeux and D. Solgadi, *Chem. Phys.* 94 (1985) 247.
- [31] M. Nonella and J.R. Huber, *Chem. Phys. Letters* 131 (1986) 376.
- [32] S. Hennig, V. Engel, R. Schinke, M. Nonella and J.R. Huber, *J. Chem. Phys.* 87 (1987) 3522.
- [33] A. Ticktin, A.E. Bruno, U. Brühlmann and J.R. Huber, *Chem. Phys.* 125 (1988) 403.
- [34] H. Okabe, *Photochemistry of Small Molecules* (Wiley, New York, 1978).
- [35] K.G. McKendrick, D.J. Rakestraw and R.N. Zare, *Faraday Discussions Chem. Soc.* 84 (1987) 39.
- [36] K.G. McKendrick, D.J. Rakestraw, R. Zhang and R.N. Zare, *J. Phys. Chem.* 92 (1988) 5530.
- [37] H. Zacharias, M. Geilhaupt and K.H. Welge, *J. Chem. Phys.* 74 (1981) 218.